

SkullGAN: Synthetic Skull CT Generation with Generative Adversarial Networks

Kasra Naftchi-Ardebili^{1,†}, Karanpartap Singh^{2,3,†}, Reza Pourabolghasem, Pejman Ghanouni³,
Gerald R. Popelka^{3,4}, Kim Butts Pauly^{1,2,3}

¹Department of Bioengineering, Stanford University, Stanford, CA, 94301

²Department of Electrical Engineering, Stanford University, Stanford, CA, 94301

³Department of Radiology, Stanford University, Stanford, CA, 94301

⁴Department of Otolaryngology, Stanford University, Stanford, CA, 94301

Manuscript Type: Original Research Article

Funding: This work was generously supported by NIH R01 Grant EB032743.

Word Count: 3131

Acknowledgments: We would like to thank Jeremy Irvin and Eric Luxenberg for their helpful discussions, Ningrui Li and Fanrui Fu for advice on skull CT segmentation and preprocessing, and Jeff Elias at The University of Virginia for graciously providing 28 of the 38 human skull CTs for training SkullGAN.

This work has been submitted to *Radiology: Artificial Intelligence* for possible publication. Copyright may be transferred without notice, after which this version may no longer be accessible.

arXiv:2308.00206v1 [eess.IV] 1 Aug 2023

Corresponding Author: knaftchi@stanford.edu

† These authors contributed equally to this work.

SkullGAN: Synthetic Skull CT Generation with Generative Adversarial Networks

Original Research Article submitted July 9, 2023

Summary

SkullGAN, a deep generative adversarial network, can generate large numbers of synthetic skull CT segments that are visually and quantitatively indistinguishable from real skull CT segments for training deep learning models with applications in healthcare.

Key Points

- To address limitations in accessing large numbers of real, curated, and anonymized skull CTs to train deep learning models involving the human skull, SkullGAN was trained on 2,414 normal, real skull CT segments from 38 subjects to generate highly varied synthetic skull images.
- Synthetic CT images generated by SkullGAN were indistinguishable from a test set of real skull CTs, both in quantitative radiological metrics and when subject to the SkullGAN discriminator.
- Radiological metrics such as skull density ratio (SDR) can easily be fooled if used for statistical comparison between real and synthetic skulls. Many-parameter nonlinear classifiers are better suited for separating low quality slices from realistic ones.

Abstract

Purpose: Deep learning offers potential for various healthcare applications involving the human skull, yet requires extensive datasets of curated medical images. To overcome this challenge, we propose SkullGAN, a generative adversarial network (GAN), to create large datasets of synthetic skull CT slices, thus reducing reliance on real images and accelerating the integration of machine learning into healthcare.

Materials and Methods: CT slices of 38 subjects were fed to SkullGAN, a neural network comprising over 200 million parameters. The generated synthetic skull images were then evaluated based on three quantitative radiological features: skull density ratio (SDR), mean thickness, and mean intensity. They were further analyzed using t-distributed stochastic neighbor embedding (t-SNE), and by applying the SkullGAN discriminator as a classifier.

Results: SkullGAN-generated images demonstrated similar key quantitative radiological features to real skulls. Additionally, more definitive analysis was undertaken by applying the discriminator of SkullGAN. The SkullGAN discriminator classified 56.5% of a test set of real skull images and 55.9% of the SkullGAN-generated images as reals (the theoretical optimum being 50%), demonstrating that the SkullGAN-generated skull set is indistinguishable from the real skull set – within the limits of our nonlinear classifier.

Conclusion: SkullGAN makes it possible for researchers to generate large numbers of synthetic skull CT segments, necessary for training neural networks for medical applications involving the human skull. By doing so, it mitigates challenges associated with preparing large, high-quality training datasets, such as access, capital, time, and the need for domain expertise.

Introduction

The adequate training of a neural network requires very large and often difficult to obtain quantities of standardized data. This problem becomes even more pronounced in medical applications where data preparation steps such as anonymizing, slicing, segmentation, pre-processing, and labeling cannot be easily crowdsourced and require domain expertise [1, 2, 3]. To address this data scarcity problem in medical applications involving human skull imaging, we propose SkullGAN, a deep Generative Adversarial Network (GAN) that generates large numbers of synthetic skull CT segments for training deep learning models and for simulation software. We will investigate whether SkullGAN-generated skull CT segments display visual similarities to real skull CTs without being exact replicas of the training set, and if they are quantitatively indistinguishable from a test set of real skull CTs.

Related Work

The limited availability of sufficiently large datasets, on the order of thousands of samples, of preprocessed and segmented human skull CTs has never been addressed via generative methods. Insofar as other systems and organs are concerned, prior research in exploring GANs for creating synthetic medical images such as cardiac MRI, liver CT, and retina images showed that their generated samples did not have the same richness as real images [4]. More than being a critique of the power of GANs, this prior work was a critique of the reliability of traditional evaluation metrics, such as the Fréchet inception distance score [5], in assessing the quality of GAN-generated samples. In a separate work where GAN-generated liver lesions were used to augment available real medical images for training purposes, their convolutional neural network classification performance improved from 78.6% to 85.5% in sensitivity and from 88.4% to 92.4% in specificity [6]. These findings point to the potential GANs hold in generating synthetic medical images that could effectively replace real medical images for training neural networks, if enough capacity is given to the networks and adequate curated data is used to train them.

Materials and Methods

Model

SkullGAN is based on the Generative Adversarial Network (GAN) [7] and the deep-convolutional GAN (DC-GAN) [8]. We augment the DC-GAN architecture with two noise-injection layers. This simple modification helps SkullGAN produce high-quality 128×128 skull CT segments.

Following the original implementation, we use binary cross entropy loss with the following loss function:

$$\ell = \log D(x) + \log(1 - D(G(z))), \quad (1)$$

where x is a real skull segment sample and z is a random noise vector sampled from a uniform distribution, with $D(\cdot)$ and $G(\cdot)$ denoting the discriminator and generator, respectively.

Network Architecture

The generator, shown in Figure 1, takes a latent vector of size 200 as input and passes it through 6 sequential 2D convolutional layers. The output of the first layer has 4,096 channels, with each subsequent layer downscaling the channels by a factor of two and upscaling the features by a factor of two to yield an intermediate output of $128 \times 128 \times 128$. Subsequent convolutional layers reduce the channel dimension to yield a final output of size $1 \times 128 \times 128$. External information in the form of Gaussian noise is injected into two layers of the generator to improve the quality of the pore structures in the generated skulls. A tanh layer constrains the final output to $[-1, 1]$, to match the normalization used for the training set. The discriminator has a mirrored

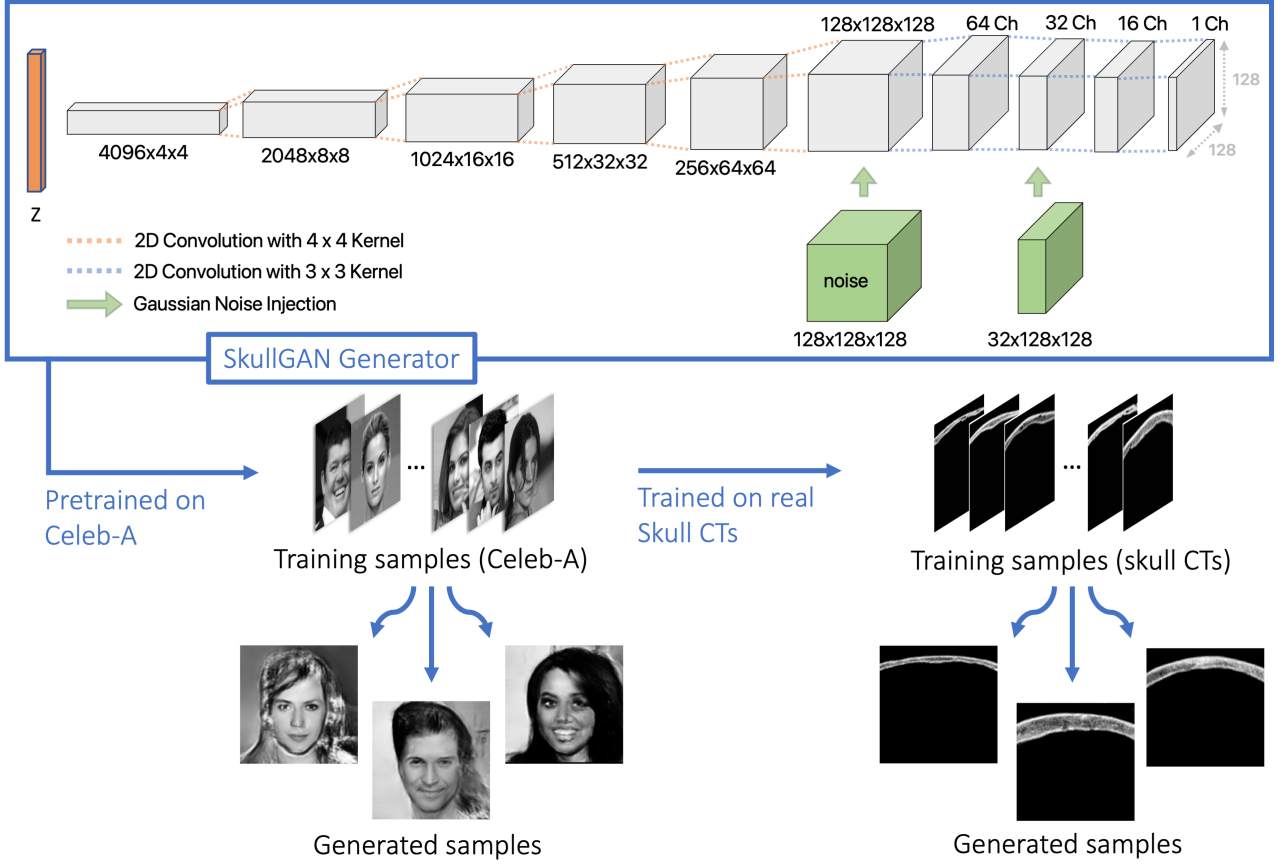


Fig. 1 | SkullGAN generator and training pipeline. SkullGAN was first pre-trained on the Celeb-A dataset, and then trained on human skull CTs. In contrast to random initialization of the weights for training on the human skull CTs, pre-training yielded layers with fine-tuned weights for detecting edges and resulted in better quality skull segment images, with finer definition both in contour and interior bone structure.

architecture without Gaussian noise injection. These conditions result in 192 million parameters in the generator and 11.2 million parameters in the discriminator. Layer details are presented in Table 1.

CT Imaging and Segmentation

This study included 38 anonymized skull CT scans from healthy subjects, with 28 from the University of Virginia’s Department of Radiology and 10 from Stanford’s Department of Radiology. All CT scans were taken at 120 keV on GE scanners with axial slicing, a 0.625 mm slice thickness, and the Bone Plus kernel.

The skull CTs were segmented using ImageJ and Slicer [9, 10] to remove the brain and artifacts outside the skull. Slices were selected at an interval of 3.1 mm (every 5 slices) in the axial, coronal, and sagittal planes. As such, our training set consisted of slices from the temporal and parietal bones. Given the high variability in skull structure within subjects, both the left and the right temporal bones were extracted from every axial plane, without fear of biasing the dataset. Conversely, irregularities and sutures present in the frontal and occipital bones, combined with the small size of our training dataset, diminished the quality of the SkullGAN-generated skull segments. As such, we excluded frontal and occipital bones from the training set. Slices were

masked in MATLAB [11] to produce a final dataset of 4,828 2D skull segments, half of which were used for training and half for testing (Figure 2).

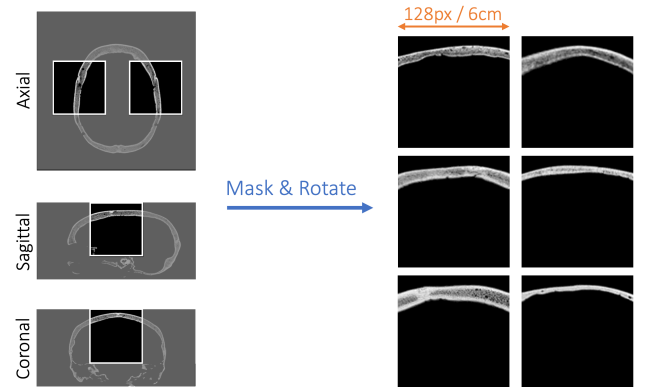


Fig. 2 | SkullGAN training set preparation. After segmentation, the slices were masked and rotated where necessary. To account for both the left and the right temporal bones, two segments were taken from each axial slice. This resulted in a training set of 2,414 2D horizontal skull segments.

| Generator | | | | Discriminator | | | |
|-------------|-----------------------|--|-----------------------------|---------------|----------------------|--|---------------------------|
| Layers | | Specifications | Output Size | Layers | | Specifications | Output Size |
| Block 1 | Transpose Convolution | 4×4 conv, stride 1, padding 0 | $4096 \times 4 \times 4$ | Block 1 | Convolution | 4×4 conv, stride 2, padding 1 | $64 \times 64 \times 64$ |
| | Batch Normalization | momentum 0.1 | | | Leaky ReLU | negative slope 0.2 | |
| | ReLU | none | | | Convolution | 4×4 conv, stride 2, padding 1 | |
| Block 2 | Transpose Convolution | 4×4 conv, stride 2, padding 1 | $2048 \times 8 \times 8$ | Block 2 | Batch Normalization | momentum 0.1 | $128 \times 32 \times 32$ |
| | Batch Normalization | momentum 0.1 | | | Leaky ReLU | negative slope 0.2 | |
| | ReLU | none | | | Convolution | 4×4 conv, stride 2, padding 1 | |
| Block 3 | Transpose Convolution | 4×4 conv, stride 2, padding 1 | $1024 \times 16 \times 16$ | Block 3 | Batch Normalization | momentum 0.1 | $256 \times 16 \times 16$ |
| | Batch Normalization | momentum 0.1 | | | Leaky ReLU | negative slope 0.2 | |
| | ReLU | none | | | Convolution | 4×4 conv, stride 2, padding 1 | |
| Block 4 | Transpose Convolution | 4×4 conv, stride 2, padding 1 | $512 \times 32 \times 32$ | Block 4 | Batch Normalization | momentum 0.1 | $512 \times 8 \times 8$ |
| | Batch Normalization | momentum 0.1 | | | Leaky ReLU | negative slope 0.2 | |
| | ReLU | none | | | Convolution | 4×4 conv, stride 2, padding 1 | |
| Block 5 | Transpose Convolution | 4×4 conv, stride 2, padding 1 | $256 \times 64 \times 64$ | Block 5 | Batch Normalization | momentum 0.1 | $1024 \times 4 \times 4$ |
| | Batch Normalization | momentum 0.1 | | | Leaky ReLU | negative slope 0.2 | |
| | ReLU | none | | | Convolution | 4×4 conv, stride 1, padding 0 | |
| Block 6 | Transpose Convolution | 4×4 conv, stride 2, padding 1 | $128 \times 128 \times 128$ | Block 6 | Convolution | 4×4 conv, stride 1, padding 0 | 1×1 |
| Block 7 | Convolution | 3×3 conv, stride 1, padding 1 | $64 \times 128 \times 128$ | | | | |
| | Convolution | 3×3 conv, stride 1, padding 1 | $32 \times 128 \times 128$ | | | | |
| | Convolution | 3×3 conv, stride 1, padding 1 | $16 \times 128 \times 128$ | | | | |
| | Convolution | 3×3 conv, stride 1, padding 1 | $1 \times 128 \times 128$ | | | | |
| Final Layer | Normalizing Layer | Hyperbolic Tangent | $1 \times 128 \times 128$ | Final Layer | Classification Layer | Sigmoid | 1×1 |

Table 1 | Generator and discriminator architectures in SkullGAN. In the generator, Gaussian noise is added to the outputs of Block 6 and second layer of Block 7.

Datasets

The training and evaluation of SkullGAN involve multiple sets of images, each catering to unique stages in the training and assessment of the model. The first step involves pre-training SkullGAN on a large dataset of human faces to familiarize the model with facial features and structures. The main training process then trains SkullGAN on real human skull images. The output of SkullGAN is referred to as the synthetic set, which is a collection of generated skull CT images. The quality of these synthetic images is evaluated through comparison with various other image sets, each providing a unique perspective for evaluation. Example images from each set are shown in Figure 3.

pre-training set: 100,000 cropped and rescaled 128×128 celebrity images (Celeb-A dataset) [12]. This dataset, well-known in computer vision literature [13, 14], was used during pre-training to allow the model to learn fundamental facial structures and features, which facilitated its subsequent learning of human skulls during the main training phase.

training set: 2,414 real human skull CT segments used to train SkullGAN.

test set: 2,414 real human skull CT segments used for analysis and comparison to the synthetic set. These samples are distinct from the training set and were not seen by SkullGAN during training.

synthetic set: 1,000 2D synthetic skull segments generated by SkullGAN.

control set: 1,000 2D synthetic skull segments generated by a less powerful iteration of SkullGAN that did not incorporate pre-training or other enhancements in the final model. This set serves as a baseline for performance comparison, allowing us to evaluate the improvements achieved with the current iteration of SkullGAN.

artificial set: 500 *idealized* skull segments, engineered to represent the simplest model of the skull, and 500 *unrealistic* skull segments, purposefully engineered to

look ostensibly unreal. Although visually distinct from real skull images, these artificial images are designed to fool quantitative radiological metrics such as SDR, mean thickness, and mean intensity, illustrating the potential limitations of these common metrics when assessing synthetic skulls.

Training

SkullGAN was pre-trained on 100,000 Celeb-A samples [12] for 10 epochs and then trained on the training set for 1,000 epochs. Pre-training greatly improved the resolution of the synthetic set, while reducing the number of iterations required for convergence during training. The training set was normalized to a range of $[-1, 1]$. Both the generator and discriminator networks used mini-batch training with a batch size of 64. Optimization was performed using the Adam optimizer [15] with no weight decay and $\beta = 0.5$.

To stabilize the networks and improve the synthetic skulls, several techniques were applied. For the discriminator, we used label smoothing by assigning soft labels of 0.9 (instead of 1.0) for real samples to encourage stabilization. A dynamic learning rate reduction on plateau [16] was used for both networks: For the generator, a decay factor of 0.5 and patience of 1,000 iterations was determined through our parameter search, while for the discriminator, a decay factor of 0.8 and patience of 1,000 iterations were used. Each network was allowed to update only if its loss in the last batch was lower than a heuristically-determined value of 90%. Gaussian-blurred real samples were gradually introduced to the discriminator as fake samples (0 labeled) past the 15th epoch, until a ratio of $1/2$ blurred real samples and $1/2$ fake samples was reached. This ratio was then kept constant. Figure 4 illustrates the comprehensive training and inference workflows of SkullGAN, providing an explanation for the various datasets utilized in each step.

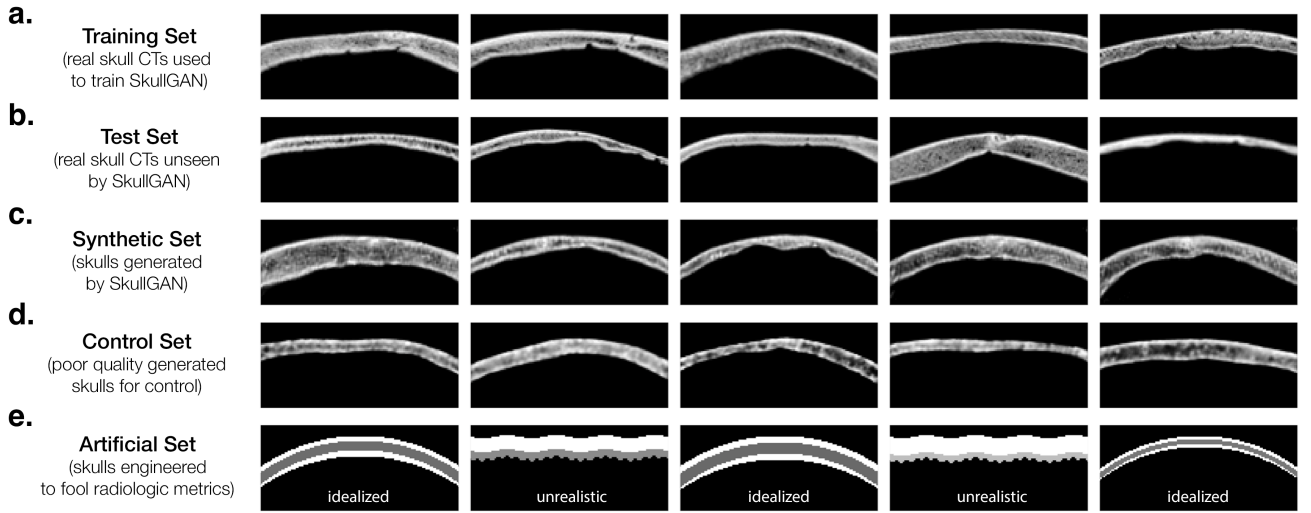


Fig. 3 | Five cropped examples from each dataset. **a.** Training Set: real skull CT segments. **b.** Test Set: real skull CT segments unseen by SkullGAN. **c.** Synthetic Set: skull CT segments generated by SkullGAN. **d.** Control Set: poor-quality skull CT segments generated by a less powerful iteration of SkullGAN that was not pretrained on the Celeb-A dataset. **e.** Artificial Set: idealized and unrealistic fake skull CT segments deliberately engineered to look unlike any real skull segments and yet fool quantitative radiological assessment metrics.

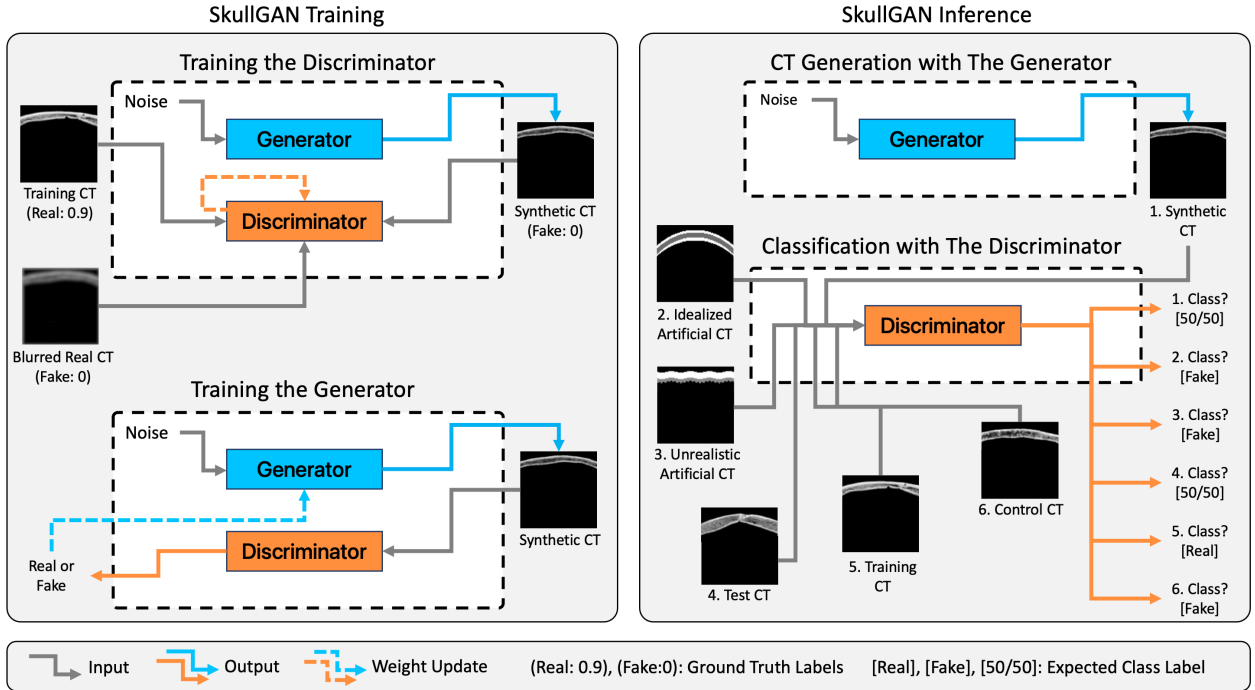


Fig. 4 | Training and Inference Workflows. **Training the Discriminator:** In each iteration, a batch of synthetic CT images (labeled 0), generated by the Generator, and a batch of real CT scans (labeled 0.9) are presented to the Discriminator. To facilitate the production of high-resolution CT scans by the Generator, we aim to enhance the Discriminator's classification ability. Thus, at every iteration, we also introduce a batch of Gaussian-blurred real CT scans, but label them as fakes (labeled 0). **Training the Generator:** The Generator creates synthetic CT scans, which are then evaluated by the Discriminator for authenticity. The weights of the generator are updated based on these evaluations. **Inference (CT Generation with the Generator):** After training, the Generator is employed to produce the synthetic set. **Inference (Classification with the Discriminator):** The trained Discriminator serves as a powerful classifier, determining whether its input is real or fake. Six distinct datasets are presented with their expected class labels in brackets. The training CTs are expected to be labeled as real, but if trained effectively, the Generator should produce synthetic CTs that the Discriminator cannot confidently classify. At this stage, a random ($50/50$) classification is anticipated. This logic also applies to the unseen test CT dataset, which is also expected to yield a $50/50$ classification.

Quantitative Radiological Metrics

Skull Density Ratio (SDR)

SDR [17] was calculated for each skull segment by taking 32 vertical cross-sections down the segment, spaced approximately 1.8 mm apart, and then computing the mean ratio of the minimum to maximum pixel intensities:

$$\text{SDR}_j = \frac{1}{32} \sum_{i=1}^{32} \frac{\min(S_{ji})}{\max(S_{ji})}, \quad (2)$$

where SDR_j denotes the SDR for skull j , and S_{ji} refers to the i^{th} vertical cross-section for the j^{th} skull segment.

Mean Thickness

The mean thickness of each skull segment was calculated by averaging the thickness through 32 cross-sections down the image, spaced approximately 1.8 mm apart:

$$\text{MT}_j = \frac{1}{32} \sum_{i=1}^{32} \rho \times T_i, \quad (3)$$

where T_i denotes the thickness in pixels of a cross-section i , and ρ denotes the CT resolution in mm/pixel .

Mean Intensity

The mean intensity for each skull segment was calculated by first thresholding the image to ignore Hounsfield Unit (HU) values of 10 or less (the background). The intensity of each pixel was then averaged to obtain the mean intensity of the skull segment:

$$\text{MI}_j = \frac{1}{N_j} \sum_{x,y} I(x,y) \cdot \mathbf{1}_{I(x,y) > 10 \text{ HU}} \quad (4)$$

where MI_j denotes the mean intensity for skull segment j , and N_j is the total number of pixels in segment j that meet the thresholding requirement of > 10 HU.

Separability of the Datasets

We used t-distributed stochastic neighbor embedding (t-SNE) [18] and the discriminator of SkullGAN to assess the similarity or separability of our datasets.

The t-SNE algorithm constructs a probability distribution for pairs of objects based on their similarity, both in the original high-dimensional space and in a lower dimensional representation, and then iteratively solves for a mapping between the two distributions, thus representing the high-dimensional objects in a lower-dimensional, visually interpretable manner.

The discriminator of SkullGAN was trained to convergence until it could no longer decisively label the generator output as real or fake. The theoretical global minimum of this minimax game is when the Discriminator reaches a 50% accuracy [7]. Therefore, if the discriminator classifies half of the test set as real and the other half as fake, and shows a similar performance on newly generated synthetic samples by SkullGAN, we

can conclude that SkullGAN generates skull segments that are quantitatively indistinguishable from test skull segments, within the limits of our discriminator’s capacity as a classifier.

Memory GAN

A common challenge in training GANs is “Memory GAN,” in which the network simply memorizes the training set [19]. To test for this failure mode and verify the uniqueness of our SkullGAN-generated segments, we compared all of our training set to an equally sized batch of our synthetic set. To find the closest real counterparts to the synthetic segments, we searched for the minimum distance between synthetic and real samples, computed once via scale-invariant feature transform (SIFT) [20], and once with simple pixel-wise mean squared error (MSE).

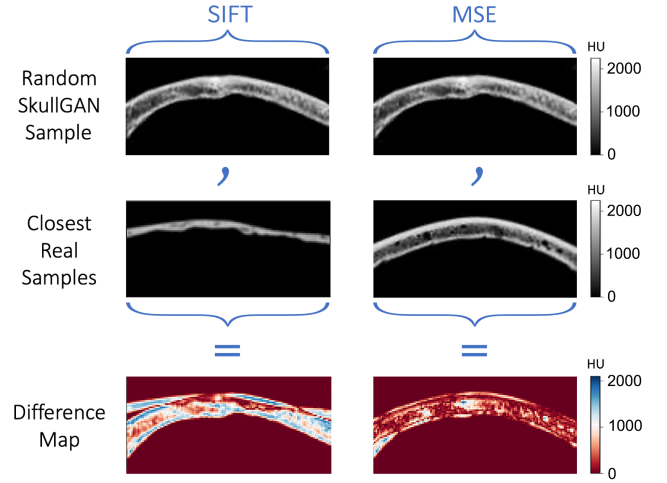


Fig. 5 | Example random SkullGAN samples, their closest real counterparts, and the difference maps between them (images cropped for visual purposes). Hounsfield unit values of 0 correspond to water, and above 700 to bone [21].

Results

Figure 3 displays example images from the training set, the test set, the synthetic set generated by SkullGAN, the poor quality control set generated by a less powerful version of SkullGAN that was not pre-trained on the Celeb-A dataset, and the artificial set, separated into idealized and unrealistic varieties. The total training time for SkullGAN was approximately 2 hours on 2 NVIDIA A100 40GB GPUs, running on a machine-learning optimized Google Cloud Platform [22] instance. Generation time on this setup averaged 2.95 seconds for 2,500 images and 9.6 minutes for 100,000 images.

Memory GAN

We employed two methods in identifying whether the generator in SkullGAN was overfitting the training set:

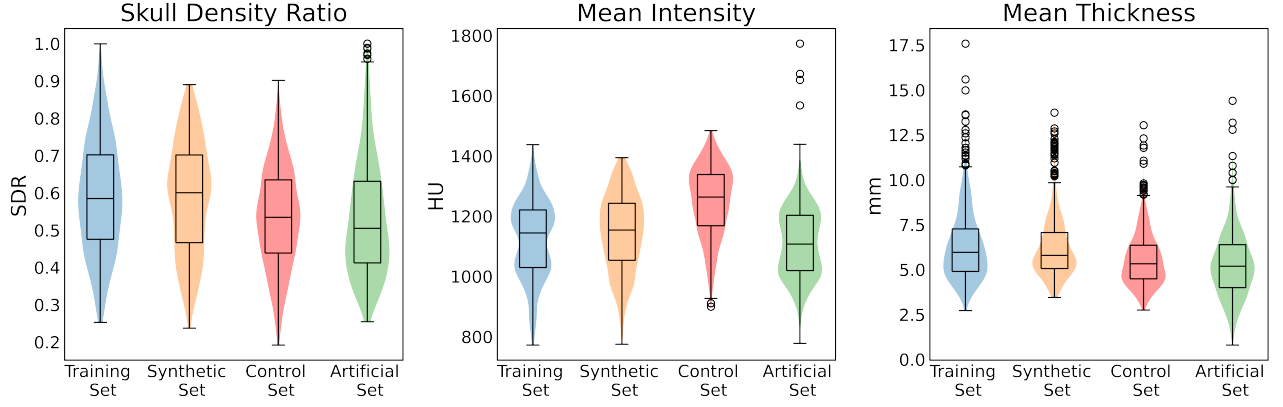


Fig. 6 | Violin plots of the quantitative radiological metrics for the training, synthetic, control, and artificial sets. What is noteworthy is that we can engineer artificial skulls that are ostensibly unrealistic and still match the training set (real skull CTs) across the three radiological metrics of skull density ratio, mean intensity, and mean thickness. In fact, we can go as far as matching the shapes of the distributions: the bimodal distribution of mean intensity for the artificial set resembles that of the training set.

pixel-wise MSE and SIFT. We found the candidates identified through pixel-wise MSE to be visually more similar to one another, compared to candidates identified through SIFT. Example of differences in pixel intensities for both metrics are shown in Figure 5. None of the randomly generated samples were replicas of their closest real counterparts, allowing the conclusion that the SkullGAN network did not memorize the training set.

Susceptibility of the Quantitative Radiological Metrics to Failure

While quantitative radiological metrics such as SDR, mean thickness, and mean intensity are viable measures to compare real skull CTs for the purpose of clinical evaluation, they can fail when assessing synthetic skull CTs. As shown in Figure 6, artificial skull CT segments engineered to match the SDR, mean thickness, and mean intensity distributions of real skull CT segments can easily fool these metrics, even though they are visually clearly fake. Therefore, more powerful methods were employed to analyze the separability of these datasets.

Visual Clustering of Skull Data Sets

When applying t-SNE to the distributions of radiologic metrics for all of the data points (Figure 6), we observed no separability, confirming the inadequacy of these features in authenticating the real skull CT segments from the synthetic and artificial sets (Figure 7a). However, once we break free from these limiting radiological metrics and instead unroll every sample into a vector of length 128×128 , t-SNE treats every entry (pixel) in this vector as a feature. Applying t-SNE to the $4,000 \times 16,384$ matrix where the rows represent training, control, synthetic, and artificial skull sets in batches of 1,000, we observed a clear separate clustering of the artificial set. Interestingly, within the artificial set, the unrealistic segments were in a clearly

separate cluster than the idealized segments (Figure 7b). Despite this, t-SNE still fell short of separating the training set from the control set and the synthetic (SkullGAN-generated) set. A more complex, highly nonlinear classifier, in this case the SkullGAN discriminator, was needed to separate these similar distributions.

Classification by the Discriminator

Unlike the typical radiological metrics or t-SNE, the discriminator successfully separated the datasets into groups anticipated *a priori*. As demonstrated in Figure 7c, the discriminator classified 97.1% of the training set, 56.5% of the test set, and 55.9% of the SkullGAN-generated synthetic set as real. 100% classification of the training set as reals was not expected, especially because Gaussian-blurred reals were introduced as fakes during training. While t-SNE failed to separate the control set from the training and synthetic sets, the discriminator correctly classified 100% of the control set as fakes (Figure 7b,c). Labeling the artificial set as fake was no difficult task for the discriminator as evidenced by the clustering of the artificial set in the leftmost end of the classification spectrum.

Discussion

In this work, we demonstrated the ability of SkullGAN to generate large numbers of synthetic skull CT segments that are visually and quantitatively indistinguishable from real skull CTs. One of the main advantages of using SkullGAN is its ability to overcome some of the challenges associated with obtaining real CT scans. Large datasets of anonymized, curated, and preprocessed medical images often are limited by factors such as time, capital, and access. In contrast, SkullGAN can generate an infinite number of highly varied skull CT segments quickly and at a very low cost. This makes it possible for any researcher to generate

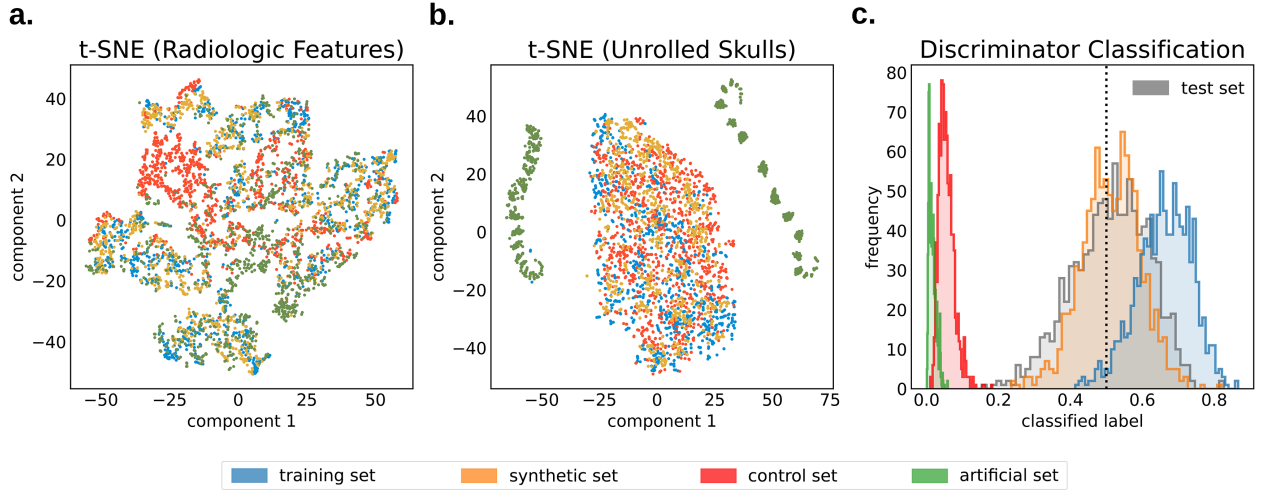


Fig. 7 | Separability of the datasets. **a.** Visual representation of t-SNE applied to the radiological features shown in Figure 6. No discernible clustering is seen, and the datasets appear inseparable with this method. **b.** Visual representation of t-SNE applied to the unrolled skulls, where each image is represented as a vector of size 16,384. The artificial set is clearly separated into clusters by t-SNE (one for the unrealistic models and another for the idealized models), while the other distributions remain inseparable. **c.** Classifications of each dataset by the SkullGAN discriminator. The dotted line represents the 0.5 mark. Data points labeled ≥ 0.5 are classified as real, and data points labeled < 0.5 are classified as fake. A large proportion of the training dataset is classified as real (97.1%), while the entirety of the control and artificial sets are confidently classified as fakes. Results from SkullGAN and a test set of 2,414 real skulls yield a near 50/50, or random guess by the model. (Note that **a** and **b** did not have a test set, hence the absence of test set in the horizontal legend.)

large datasets of skull CT segments for the purpose of training deep-learning models with applications involving the human skull, geared towards medical diagnosis and treatment planning.

One such example is the field of transcranial ultrasound stimulation (TUS), where convergent, high frequency sound waves sonicate a target deep within the brain, transcranially and noninvasively [23, 24, 25]. TUS holds the potential for treatment of a wide range of neurological disease [26, 27, 28, 29, 30]. Even though accounting and correcting for beam aberrations as they pass through the skull and intersect at a target inside the brain [31, 32, 33], lends itself to being cast as an end-to-end machine learning problem, there have been little to no such attempts to date [34, 35]. Such a machine learning model would be able to plan ultrasound treatments much faster than conventional methods while offering higher accuracy. The main reason such a model hasn't been attempted is a lack of a sufficiently large dataset of preprocessed real human skull CTs for the purposes of training neural networks. When large samples of skull CTs were needed, either manually preprocessed human skull scans [36], or idealized models had been simulated [34, 37]. However, we showed that idealized skulls can only fool quantitative radiological metrics, but cannot deceive a powerful nonlinear classifier. As such, these artificial skulls would be unlikely to yield high performance for supervised learning models. Instead of resorting to these idealized representations of skulls, researchers can now use SkullGAN to test their algorithms on large quantities of realistic synthetic skull CT segments.

There are some challenges associated with evaluating the quality of the synthetic CT scans generated by

SkullGAN. As mentioned earlier, quantitative radiological metrics such as skull density ratio (SDR), mean thickness, and mean intensity are susceptible to spurious results if used for statistical comparison between real and synthetic skulls. Instead, many-parameter nonlinear classifiers are better suited for separating low-quality slices from realistic ones. Here, we demonstrated the inseparability of our synthetic set from a test set by applying our discriminator as a classifier.

One potential limitation of this work is that we have trained SkullGAN on a relatively small dataset of 38 subjects. While the results are promising, it would be useful to test this technique on a larger and more diverse dataset to ensure that it generalizes well to other populations. A larger dataset, on the order of hundreds of real human skull CTs, would further improve the quality of the synthetic skull images.

Additionally, our primary application for developing SkullGAN was TUS. In TUS, ultrasound transducers are typically placed either on temporal bone or parietal bone. For that reason, we focused on training SkullGAN to generate realistic temporal and parietal bones. With the rise of application-specific demand for other parts of the skull, retraining of SkullGAN over a dataset that includes occipital and frontal lobes will be necessary.

Another limitation of the present study is that SkullGAN only generates 2D slices of skull CT segments. While this is suitable for some applications, it is not yet ideal for clinical deep-learning algorithms. Additionally, the 2D nature of SkullGAN means that it may not capture certain features of the skull that are only visible in three dimensions, such as complex bone structures or variations in bone density. Future work could

explore the possibility of extending SkullGAN to generate 3D volumetric skull CT scans. Another potential avenue could be exploring the use of a 2.5D model for generating pseudo-volumetric images [38, 39]. This approach involves generating 2D slices of the object of interest and then stacking them together to create a 3D image. While not a true volumetric image, this approach can provide some of the benefits of 3D imaging while still leveraging the strengths of SkullGAN’s 2D approach. This could be a promising direction for researchers looking to generate synthetic medical images for use in deep-learning models that require 3D data, but for whom obtaining sufficient volumetric data is not feasible.

In conclusion, our work presents a novel approach of using GANs to address data scarcity problems in healthcare, by generating large numbers of synthetic human skull CT segments. The results demonstrate that SkullGAN is capable of generating synthetic skull CT segments that are indistinguishable from real skull CT segments. Future work should investigate the performance of SkullGAN on larger and more diverse datasets, and extend SkullGAN to generate volumetric skull models. Much like ImageNet [40] played a pivotal role in development of advanced deep learning algorithms in computer vision, by providing a very large labeled dataset for training, SkullGAN and its variants trained on other systems and organs of the human body [6, 41, 4] may play a similar role. The preponderance of such valid, high-quality, and preprocessed medical images readily available to any researcher will usher in a new wave of advanced deep learning models in healthcare, that go beyond classification and segmentation.

Acknowledgements

We would like to thank Jeremy Irvin and Eric Luxenberg for their helpful discussions, Ningrui Li and Fanrui Fu for advice on skull CT segmentation and pre-processing, and Jeff Elias at The University of Virginia for graciously providing 28 of the 38 human skull CTs for training SkullGAN. This work was generously supported by NIH R01 Grant EB032743.

Code Availability

SkullGAN was written in Python v3.9.2 using PyTorch v1.9.0. All of the source code and training data are available at <https://github.com/kbp-lab/SkullGAN>.

References

- [1] G. Litjens, T. Kooi, B. E. Bejnordi, A. A. A. Setio, F. Ciompi, M. Ghafoorian, J. A. van der Laak, B. van Ginneken, and C. I. Sánchez, “A survey on deep learning in medical image analysis,” 2017.
- [2] H. Greenspan, B. Van Ginneken, and R. M. Summers, “Guest Editorial Deep Learning in Medical Imaging: Overview and Future Promise of an Exciting New Technique,” 2016.
- [3] H. R. Roth, L. Lu, J. Liu, J. Yao, A. Seff, K. Cherry, L. Kim, and R. M. Summers, “Improving Computer-Aided Detection Using Convolutional Neural Networks and Random View Aggregation,” *IEEE Transactions on Medical Imaging*, vol. 35, no. 5, 2016.
- [4] Y. Skandarani, P.-M. Jodoin, and A. Lalonde, “GANs for Medical Image Synthesis: An Empirical Study,” 5 2021.
- [5] M. Heusel, H. Ramsauer, T. Unterthiner, B. Nessler, and S. Hochreiter, “GANs trained by a two time-scale update rule converge to a local Nash equilibrium,” in *Advances in Neural Information Processing Systems*, vol. 2017-December, 2017.
- [6] M. Frid-Adar, I. Diamant, E. Klang, M. Amitai, J. Goldberger, and H. Greenspan, “GAN-based synthetic medical image augmentation for increased CNN performance in liver lesion classification,” *Neurocomputing*, vol. 321, 2018.
- [7] I. J. Goodfellow, J. Pouget-Abadie, M. Mirza, B. Xu, D. Warde-Farley, S. Ozair, A. Courville, and Y. Bengio, “Generative adversarial nets,” in *Advances in Neural Information Processing Systems*, vol. 3, 2014.
- [8] A. Radford, L. Metz, and S. Chintala, “Deep Convolutional Generative Adversarial Networks (DCGAN),” *4th International Conference on Learning Representations, ICLR 2016 - Conference Track Proceedings*, 2016.
- [9] C. A. Schneider, W. S. Rasband, and K. W. Eliceiri, “NIH Image to ImageJ: 25 years of image analysis,” 2012.
- [10] A. Fedorov, R. Beichel, J. Kalpathy-Cramer, J. Finet, J. C. Fillion-Robin, S. Pujol, C. Bauer, D. Jennings, F. Fennessy, M. Sonka, J. Buatti, S. Aylward, J. V. Miller, S. Pieper, and R. Kikinis, “3D Slicer as an image computing platform for the Quantitative Imaging Network,” *Magnetic Resonance Imaging*, vol. 30, no. 9, 2012.
- [11] “MATLAB version 9.10.0.1613233 (R2021a),” 2021.
- [12] Z. Liu, P. Luo, X. Wang, and X. Tang, “Large-scale celebfaces attributes (celeba) dataset,” *Retrieved August*, vol. 15, 2018.
- [13] J. Yu, Z. Lin, J. Yang, X. Shen, X. Lu, and T. S. Huang, “Generative Image Inpainting with Contextual Attention,” in *Proceedings of the IEEE Computer Society Conference on Computer Vision and Pattern Recognition*, 2018.
- [14] Q. Feng, C. Guo, F. Benitez-Quiroz, and A. Martinez, “When do GANs replicate? On the choice of dataset size,” in *Proceedings of the IEEE International Conference on Computer Vision*, 2021.
- [15] D. P. Kingma and J. L. Ba, “Adam: A method for stochastic optimization,” in *3rd International Conference on Learning Representations, ICLR 2015 - Conference Track Proceedings*, 2015.
- [16] PyTorch, “PyTorch documentation - PyTorch master documentation,” 2019.
- [17] K. W. K. Tsai, J. C. Chen, H. C. Lai, W. C. Chang, T. Taira, J. W. Chang, and C. Y. Wei, “The Distribution of Skull Score and Skull Density Ratio in Tremor Patients for MR-Guided Focused Ultrasound Thalamotomy,” *Frontiers in Neuroscience*, vol. 15, 2021.

- [18] L. van der Maaten and G. Hinton, "Visualizing Data using t-SNE," *Journal of Machine Learning Research*, vol. 9, no. 86, pp. 2579–2605, 2008.
- [19] V. Nagarajan, C. Raffel, and I. J. Goodfellow, "Theoretical Insights into Memorization in GANs," *Integration of Deep Learning Theories Workshop, 32nd Conference on Neural Information Processing Systems (NeurIPS 2018)*, 2019.
- [20] D. G. Lowe, "Object recognition from local scale-invariant features," in *Proceedings of the IEEE International Conference on Computer Vision*, vol. 2, 1999.
- [21] R. Bibb, D. Eggbeer, and A. Paterson, *Medical Modelling: The Application of Advanced Design and Rapid Prototyping Techniques in Medicine: Second Edition*. 2015.
- [22] Google Cloud Platform (GCP), "Google Cloud Platform (GCP)," 2019.
- [23] T. Zhang, N. Pan, Y. Wang, C. Liu, and S. Hu, "Transcranial Focused Ultrasound Neuromodulation: A Review of the Excitatory and Inhibitory Effects on Brain Activity in Human and Animals," *Frontiers in Human Neuroscience*, vol. 15, 9 2021.
- [24] W. Lee, H. C. Kim, Y. Jung, Y. A. Chung, I. U. Song, J. H. Lee, and S. S. Yoo, "Transcranial focused ultrasound stimulation of human primary visual cortex," *Scientific Reports*, vol. 6, 2016.
- [25] P. Ghanouni, K. B. Pauly, W. J. Elias, J. Henderson, J. Sheehan, S. Monteith, and M. Wintermark, "Transcranial MRI-guided focused ultrasound: A review of the technologic and neurologic applications," *American Journal of Roentgenology*, vol. 205, no. 1, 2015.
- [26] K.-H. Choi and J.-H. Kim, "Therapeutic Applications of Ultrasound in Neurological Diseases," *Journal of Neurosonology and Neuroimaging*, vol. 11, no. 1, 2019.
- [27] G. Leinenga, C. Langton, R. Nisbet, and J. Götz, "Ultrasound treatment of neurological diseases-current and emerging applications," 2016.
- [28] R. J. Piper, M. A. Hughes, C. M. Moran, and J. Kandasamy, "Focused ultrasound as a non-invasive intervention for neurological disease: a review," 2016.
- [29] W. J. Elias, N. Lipsman, W. G. Ondo, P. Ghanouni, Y. G. Kim, W. Lee, M. Schwartz, K. Hynynen, A. M. Lozano, B. B. Shah, D. Huss, R. F. Dallapiazza, R. Gwinn, J. Witt, S. Ro, H. M. Eisenberg, P. S. Fishman, D. Gandhi, C. H. Halpern, R. Chuang, K. Butts Pauly, T. S. Tierney, M. T. Hayes, G. R. Cosgrove, T. Yamaguchi, K. Abe, T. Taira, and J. W. Chang, "A Randomized Trial of Focused Ultrasound Thalamotomy for Essential Tremor," *New England Journal of Medicine*, vol. 375, no. 8, 2016.
- [30] P. S. Fishman and V. Frenkel, "Focused Ultrasound: An Emerging Therapeutic Modality for Neurologic Disease," *Neurotherapeutics*, vol. 14, no. 2, 2017.
- [31] M. Fink, "Time Reversal of Ultrasonic Fields—Part I: Basic Principles," *IEEE Transactions on Ultrasonics, Ferroelectrics, and Frequency Control*, vol. 39, no. 5, 1992.
- [32] A. Kyriakou, E. Neufeld, B. Werner, M. M. Paulides, G. Szekely, and N. Kuster, "A review of numerical and experimental compensation techniques for skull-induced phase aberrations in transcranial focused ultrasound," *International journal of hyperthermia : the official journal of European Society for Hyperthermic Oncology, North American Hyperthermia Group*, vol. 30, pp. 36–46, 2 2014.
- [33] S. A. Leung, T. D. Webb, R. R. Bitton, P. Ghanouni, and K. Butts Pauly, "A rapid beam simulation framework for transcranial focused ultrasound," *Scientific Reports*, vol. 9, no. 1, 2019.
- [34] A. Stanzola, S. R. Arridge, B. T. Cox, and B. E. Treeby, "A Helmholtz equation solver using unsupervised learning: Application to transcranial ultrasound," *Journal of Computational Physics*, vol. 441, 2021.
- [35] M. Shin, Z. Peng, H.-J. Kim, S.-S. Yoo, and K. Yoon, "Multivariable-Incorporating Super-Resolution Convolutional Neural Network for Accurate Transcranial Ultrasound Simulation," *TechRxiv. Preprint*, 2023.
- [36] M. Miscouridou, J. A. Pineda-Pardo, C. J. Stagg, B. E. Treeby, and A. Stanzola, "Classical and Learned MR to Pseudo-CT Mappings for Accurate Transcranial Ultrasound Simulation," *IEEE Transactions on Ultrasonics, Ferroelectrics, and Frequency Control*, vol. 69, pp. 2896–2905, 10 2022.
- [37] M. Hayner and K. Hynynen, "Numerical analysis of ultrasonic transmission and absorption of oblique plane waves through the human skull," *The Journal of the Acoustical Society of America*, vol. 110, no. 6, 2001.
- [38] A. Ziabari, D. H. Ye, S. Srivastava, K. D. Sauer, J. B. Thibault, and C. A. Bouman, "2.5D Deep Learning for CT Image Reconstruction Using A Multi-GPU Implementation," in *Conference Record - Asilomar Conference on Signals, Systems and Computers*, vol. 2018-October, 2019.
- [39] Q. Huang, Z. Zeng, and X. Li, "2.5-D Extended Field-of-View Ultrasound," *IEEE Transactions on Medical Imaging*, vol. 37, no. 4, 2018.
- [40] J. Deng, W. Dong, R. Socher, L.-J. Li, Kai Li, and Li Fei-Fei, "ImageNet: A large-scale hierarchical image database," in *2009 IEEE Conference on Computer Vision and Pattern Recognition*, pp. 248–255, IEEE, 6 2009.
- [41] C. Baur, S. Albarqouni, and N. Navab, "Generating highly realistic images of skin lesions with GANs," in *Lecture Notes in Computer Science (including subseries Lecture Notes in Artificial Intelligence and Lecture Notes in Bioinformatics)*, vol. 11041 LNCS, 2018.